



Kent Academic Repository

Jeyaranjan, Aadithya, Sakthivel, Tamil Selvan, Molinari, Marco, Sayle, Dean C. and Seal, Sudipta (2018) *Morphology and Crystal Planes Effects on Supercapacitance of CeO₂ Nanostructures: Electrochemical and Molecular Dynamics Studies*. *Particle & Particle Systems Characterization*, 35 (10). ISSN 0934-0866.

Downloaded from

<https://kar.kent.ac.uk/68743/> The University of Kent's Academic Repository KAR

The version of record is available from

<https://doi.org/10.1002/ppsc.201800176>

This document version

Author's Accepted Manuscript

DOI for this version

Licence for this version

UNSPECIFIED

Additional information

Versions of research works

Versions of Record

If this version is the version of record, it is the same as the published version available on the publisher's web site. Cite as the published version.

Author Accepted Manuscripts

If this document is identified as the Author Accepted Manuscript it is the version after peer review but before type setting, copy editing or publisher branding. Cite as Surname, Initial. (Year) 'Title of article'. To be published in *Title of Journal*, Volume and issue numbers [peer-reviewed accepted version]. Available at: DOI or URL (Accessed: date).

Enquiries

If you have questions about this document contact ResearchSupport@kent.ac.uk. Please include the URL of the record in KAR. If you believe that your, or a third party's rights have been compromised through this document please see our [Take Down policy](https://www.kent.ac.uk/guides/kar-the-kent-academic-repository#policies) (available from <https://www.kent.ac.uk/guides/kar-the-kent-academic-repository#policies>).

DOI: 10.1002/ ((please add manuscript number))

Article type: **Full Paper**

Morphology and Crystal Planes Effects on Supercapacitance of CeO₂ Nanostructures: Electrochemical and Molecular Dynamics Studies

*Aadithya Jeyaranjan, Tamil Selvan Sakthivel, Marco Molinari, Dean C. Sayle and Sudipta Seal**

Aadithya Jeyaranjan, Dr. Tamil Selvan Sakthivel, Prof. Sudipta Seal
Advanced Material Processing and Analysis Center, Department of Materials Science and Engineering, University of Central Florida, Orlando, FL 32826, U.S.A
E-mail: sudipta.seal@ucf.edu
Dr. Marco Molinari
Department of Chemistry, University of Huddersfield, Huddersfield HD1 3DH, U.K.
Prof. Dean C.Sayle
School of Physical Sciences, University of Kent, Canterbury, Kent CT2 7NH, U.K.

Keywords: Cerium oxide, Supercapacitors, Crystal plane effects, Energy storage, Molecular dynamics simulations

Nano cerium oxide (CeO₂) is a promising supercapacitor material, but the effect of morphology on charge storage capacity remains elusive. To determine this effect, three different morphologies, nano-rods, cubes and particles are synthesized by a one-step hydrothermal process. Electrochemical evaluation through cyclic voltammetry and galvanostatic charge-discharge techniques reveals specific capacitance to be strongly dependent on the nanostructure morphology. **The highest specific capacitance in nano-rods (162.47 F g⁻¹) is due to the substantially larger surface area relative to the other two morphologies, and the predominant exposure of the highly reactive {110} and {100} planes.** At comparable surface areas, exposed crystal planes **exhibit** a profound effect on charge storage. The exposure of highly reactive {100} planes in nano-cubes induce a greater specific capacitance compared to nano-particles, which are dominated by the less reactive {111} facets. The experimental findings are supported by reactivity maps of the nanostructures generated by molecular dynamics simulations. This study indicates that supercapacitors with higher charge storage can be designed through a nanostructure morphology selection strategy.

1. Introduction

The Internet of Things (IoTs) is a network of thousands of smart sensors, actuators and other devices interconnected through a digital medium that can have dramatic impacts on our daily lives. IoTs can monitor a variety of systems like power grids, wind turbines and traffic surveillance.^[1-3] The sensors connected to these networks can work independently and in tandem with other devices to collect monitoring data that can significantly improve the overall performance of systems. More importantly, monitoring **various** crucial parameters helps to predict the failure of systems, before they can actually happen.^[4] The huge potential and remarkable applications of IoTs have led to their widespread usage.^[5] With the proliferation of these sensors and actuators, comes the concern of their energy autonomy;^[6-8] in an effort to develop green and sustainable systems, energy harvesters could be used to power them.

However, the intermittent nature of renewable energy sources mandates the use of **an** appropriate electrical energy storage device (EED) alongside the harvesters.^[9]

The nature of applications for these sensors requires EEDs with high power densities and long cycle life. Pseudocapacitors are a type of EED that stores charge by fast redox reactions. Due to the rapid surface and sub-surface redox reactions, pseudocapacitors exhibit higher energy densities than traditional electrolytic double layer capacitors (EDLCs), which work by the accumulation **of electrolyte ions onto the surface of the active material**. They also show power densities higher than conventional batteries. These advantages, combined with the very high cycle life (almost 10x that of conventional batteries), make pseudocapacitors an excellent fit to power the remote sensors and actuators, in the IoTs network. Besides being used as a standalone EED, they can also be used in combination with **batteries and other EEDs**.^[10, 11] Though RuO₂ is the gold standard for pseudocapacitor materials, the high toxicity and even higher cost has limited its large-scale commercialization.^[12, 13] As a result, other redox active metal oxides that can potentially replace RuO₂ have predominantly been tested as pseudocapacitor material; these include: MnO₂, NiO, CoO_x, V₂O₅, etc.^[14-23] However, these

metal oxides also suffer from various problems like dissolution, poor cycle life and high cost.

Besides metal oxides, various materials like metal chalcogenides, MXenes, polymers and rare earth oxides are also being tested as alternate active material for pseudocapacitors.^[24-27]

One such material- cerium oxide (CeO_2), a rare earth oxide, is gaining a lot of attention due to its surplus availability, very low toxicity, highly reversible oxidation states ($3^+/4^+$), no phase change at operational conditions and low cost.^[28-36] **Though nano CeO_2 is a relatively new supercapacitor material, its unique properties have found extensive use in a wide range of other applications;** like catalytic converters, oxygen storage, solid oxide fuel cells, and biosensors.

Although highly redox active, CeO_2 does not exhibit a 2D layered structure or have 1D tunnels in the structure, like traditional EED materials, **which provide pathways for insertion/exertion of ions.** As a result, bulk CeO_2 cannot be used to assemble a practical EED.

However, this limitation can be successfully overcome by adopting a nanostructuring strategy. Nanostructuring CeO_2 boosts its surface area to volume ratio to a very large amount.^[37, 38]

Like many other metal oxides, CeO_2 , a ceramic material, suffers from an inherently low electrical conductivity. Thus, nano CeO_2 has been used as supercapacitor material, often in combination with carbonaceous materials like graphene, reduced graphene oxide (rGO), graphene oxide, nitrogen doped reduced graphene oxide and carbon nanotubes.^[29, 30, 39-42]

Supporting CeO_2 over these carbonaceous material improves the conductivity and thereby increases charge storage. Padmanathan et al. showed that CeO_2 nanoparticles and carbon coated CeO_2 nanorods synthesized by a simple hydrothermal process exhibits a specific capacitance of 381 F g^{-1} and 400 F g^{-1} respectively.^[43] Further, doping with metals has also shown to improve the capacitance. Ag and Pt doped CeO_2 , in combination with rGO, have been shown to exhibit up to five times and ten times, respectively, higher specific capacitance over their undoped counterparts.^[31] The specific capacitance can also be improved by increasing the specific surface area. A larger specific surface area exposes more redox active

sites to the electrolyte, **thereby yielding higher charge storage**. Sandipan et al. used this strategy and synthesized CeO₂ nanostructures using a metal organic framework (MOF) sacrificial template. The obtained nanostructure retained the open structure of the template and displayed a high surface area. These MOF derived CeO₂ nanostructures, when used with KOH electrolyte, exhibited charge storage close to its theoretical capacitance (560 F g⁻¹). In case of a K₄Fe(CN)₆ doped KOH electrolyte, the same material showed a higher specific capacitance of 1204 F g⁻¹ at a current density of 0.2 A g⁻¹.^[44]

The small form factor and remote location of sensors, **in IoTs**, dictate size restrictions on the EEDs. This has directly led to the advent of micron-sized supercapacitors which use nano-sized active material for charge storage.^[45] Considering the minuscule amounts of active material used in these EEDs, it is crucial to optimize them for maximum charge storage. In light of this matter, nanostructures synthesized with highly reactive exposed crystal planes could be employed to maximize energy storage; as such nanostructures have shown enhanced performance in a variety of application.^[46-48] Recently, it has been shown that CeO₂ nanostructures dominated by highly reactive crystal planes exhibited increased oxygen storage^[49] and catalytic activity.^{[50] [51]} Thus, morphological control of CeO₂ nanostructures **will also** have an effect on electrochemical charge storage, as highly reactive planes will undergo higher redox activity. Nanostructures dominated by highly reactive planes can also display better rate capability due to the improved rate of **redox reactions**.

Recently, we reported the shape controlled synthesis of different CeO₂ nanostructures by a **one-step** hydrothermal synthesis method and also established a morphological phase diagram for the same.^[52] However, the relationship between the morphology of nanostructured CeO₂ and crystal plane effect on charge storage capacity has not yet been reported. In this regard, three different morphologies; namely, CeO₂ nano-particles (CNPs), CeO₂ nano-rods (CNRs) and CeO₂ nano-cubes (CNCs) were engineered to contain specifically exposed crystallographic planes. All of these nanostructures were synthesized through a one-step

hydrothermal process by varying the reaction temperature and the concentration of the precursors. The effects of surface area and differentially exposed planes of the nanostructures on the supercapacitance have specifically been analyzed using different electrochemical techniques. Our experimental evidence is supported by molecular dynamics models and discussed within the relevant literature.

2. Results and discussion

2.1. Structural Characterization of CeO₂ nanostructures

The XRD patterns of CNR, CNC, and CNP are shown in Figure 1 b). All the peaks in the XRD spectra were effectively indexed as (111), (200), (220), (311), (222), (400), (331), and (420) plane reflections, of the pure cubic fluorite phase (JCPDS 34-0394, space group Fm $\bar{3}$ -m). CNPs and CNRs showed broader peaks, which is associated with smaller crystal size and higher lattice strain. The sharp peaks in CNCs suggested a larger crystal size and lower lattice strain. Crystallite size of all three nanostructures was calculated using the Scherrer formula ($D = k\lambda/B\cos\theta$), where D is the mean crystallite size, k is a crystallite dependent shape factor, λ is the X-ray wavelength, B is the full width at half maximum intensity and θ is the Bragg Angle. The calculated crystallite sizes of CNRs, CNCs, and CNPs were 39.77 nm, 52.14 nm, and 27.79 nm, respectively.

Figures 1 c)-h) show the TEM and HRTEM images of the as-obtained CNP, CNR, and CNC. The uniform CNPs from Figure 1 c) displayed size ranging from 15 to 20 nm. The clear lattice fringes from the HRTEM image in Figure 1 f) can be attributed to (111) and (200) planes, which have interplanar spacings of 0.31 nm and 0.28 nm, respectively. This indicated that the CNPs were octahedral in shape enclosed by {111} and truncated by {100} facets. The CNR in Fig 1 d) exhibited lengths spanning 150–200 nm and widths of 10–20 nm. Figure 1 g) depicts an HRTEM image of a CNR revealing three lattice fringes representing the (111), (220), and (200) planes, with interplanar spacings of 0.31 nm, 0.19 nm, and 0.28 nm,

respectively. The CNRs were enclosed by (111), (220), and (200) planes and showed a 1D growth along the [110] direction. Figure 1 e) shows a TEM image of as-prepared CNCs, which displayed size ranging 20–40 nm. The HRTEM image of CNCs in Figure 1 h) shows clear (200) lattice fringes with an interplanar spacing of 0.28 nm, which suggested CNCs exposed just the {100} surfaces.

It can be seen from Figures 2 a)-c) the atomistic models of the nanostructures generated by computer simulations is in accord with our experimentally synthesized nanostructures. The CNPs exhibited an octahedral structure enclosed by eight {111} and six {100} planes. CNRs showed growth in the [110] direction and were enclosed by the {100} and {110} planes, and CNCs were bound by six {100} planes. The {100} surfaces in CeO₂ were less stable compared to {111} and may facet into {111} surfaces. Close inspection of the CNRs and CNCs revealed considerable faceting of {100} surfaces into {111} together with steps and edges. In addition, the corners were not atomistically flat; rather they also faceted to {111}. Brunauer-Emmett-Teller (BET) surface areas of the CNR, CNP and CNC were estimated to be 61.18 m² g⁻¹, 44.01 m² g⁻¹ and 38.27 m² g⁻¹ respectively. These surface area values are in good agreement with previously reported values in literature.^[49] The surface area of CNR was ~50% greater than the other morphologies, whereas, CNC and CNP had comparable surface areas. Since charge storage in supercapacitors is predominantly a surface phenomenon, the large difference in surface area implies that CNR could yield better supercapacitor performance than CNC and CNP.

2.2. Electrochemical properties of CeO₂ nanostructures

The supercapacitor performance of CNR, CNP and CNC were first analyzed by cyclic voltammetry (CV) in 3M KOH electrolyte between -0.1 V and 0.45 V at various scan rates from 5 to 100 mV s⁻¹. Figures 3 a)-c) show typical CV curves of CNR, CNP and CNC at different scan rates. A rectangular shaped CV is a characteristic feature of EDLC type charge storage.^[53] It is clear from Figure 3 a)-d) that the CV curves of all three nanostructures clearly

exhibit a non-rectangular shape, which suggests that the charge storage in CeO₂ nanostructures was predominantly pseudocapacitance.^[43] The CV curves show a pair of redox peaks which correspond to oxidation and reduction of nano CeO₂ (Ce⁴⁺ ↔ Ce³⁺). The redox process is the basis of charge storage and this mechanism can be expressed by the following **faradaic reaction**:



Besides the redox process, charge storage could be attributed to two other mechanisms when the electrode is immersed into the electrolyte: The first is the classical EDLC type charge storage. This is a **non-faradaic** mechanism that results from the accumulation of electrolyte ions onto the interface between the electrode surface and the electrolyte. The second is another **faradaic** mechanism, which is due to the reversible electrochemical adsorption of the electrolyte cations onto the electrode surface. This can be expressed as follows:



The latter two mechanisms of charge storage are restricted to the surface of the electrode. However, redox type charge storage (pseudocapacitance) is not restricted to the surfaces of the electrode material and can also occur in the sub-surface redox active sites.^[28]

A linear increase in anodic and cathodic peak current with increase in scan rate is observed from Figure S2 suggesting fast kinetics of the redox reactions. Peak shifts were also observed in the CV curves of all three morphologies. This results from the high diffusion resistance at higher scan rates, which shifts the anodic peak current slightly to the positive side and the cathodic peak current slightly to the negative side. The redox peaks clearly visible even at a high scan rate of 100 mV s⁻¹ signified fast redox reactions and high kinetic reversibility of the electrode.^[54, 55]

For the same scan rate and normalized mass, it can be observed from Figure 3 d) that the area enclosed by the CV curve is highest for CNR, which is followed by CNC and CNP. This

clearly suggested that the charge storage among the three morphologies followed the order $\text{CNR} > \text{CNC} > \text{CNP}$. From the CV curves, the specific capacitance (SC) of the electrodes can be calculated by the following equation:

$$SC = \frac{\int iv dv}{2\mu m \Delta V} \quad (3)$$

where SC is the specific capacitance (F g^{-1}), v is the potential (V), i is the response current (A) in the CV curve, μ is the scan rate (mV s^{-1}), m is the mass (g) of the active electrode material and ΔV is the potential range. The specific capacitances of CNR, CNC and CNP were 61.55 F g^{-1} , 45.30 F g^{-1} and 27.01 F g^{-1} respectively, at a scan rate of 100 mV s^{-1} and 130.20 F g^{-1} , 119.22 F g^{-1} and 63.76 F g^{-1} respectively, for a scan rate of 5 mV s^{-1} .

The specific capacitance decreases with increasing scan rate (Figure 4d). At lower scan rates, the electrolyte ions have ample time to diffuse into the electrode material. This allows for charge storage not only at the surface available redox active sites but also at the interior redox active sites in the bulk of the material, which can be attributed to the high specific capacitance.^[56, 57] However, this was not the case at higher scan rates, where the diffusion of the electrolyte K^+ ions becomes limited. The limited diffusion results in underutilization of the available redox active sites in the electro-active material, which directly translates into lower specific capacitance as charge storage is mostly limited to the surface of the electrode material.^[58]

To further understand the supercapacitor properties of the three CeO_2 morphologies, galvanostatic charge- discharge (GCD) measurements were carried out in a potential range between -0.1 V and 0.45 V . Figures 4 a)-c) show typical GCD curves of CNR, CNP and CNC at different current densities from 1 A g^{-1} to 32 A g^{-1} . It can be seen that the discharge portion of the curve first shows an iR drop, which is due to the internal resistance of active electrode material. This is followed by a small region where the potential linearly varies with time, which is due to the EDLC type charge storage. The third is a predominant non-linear region,

which is associated with pseudocapacitive charge storage.^[59-61] The specific capacitance, SC of all electrodes can be estimated from the GCD curves using equation (4).

$$SC = \frac{I\Delta t}{m\Delta V} \quad (4)$$

where I is the current (A), Δt is the discharge time (s), ΔV is the potential window (V) and m is the mass (g) of the active electrode material. The specific capacitances of CNR, CNC and CNP were 162.47 F g⁻¹, 149.03 F g⁻¹, and 97.72 F g⁻¹ at 1 A g⁻¹, and, 58.59 F g⁻¹, 50.23 F g⁻¹, and 20.52 F g⁻¹ at 32 A g⁻¹. The pattern of results obtained from GCD is in clear agreement with the results from the CV curves.

The specific capacitance decreases monotonically with an increase in current density (Figure 4 e). It can be observed from Figures 4 d) and e), the SC of CNRs was consistently much higher than other nanostructures. The highest SC in CNRs can be attributed to two factors: high surface area and exposure of highly redox active crystal planes. As stated previously, the specific surface area of CNRs was almost 50% higher than CNCs and CNPs. This high surface area implied a higher number of redox active sites were exposed to the electrolyte. This can explain the better performance of CNRs, as charge storage in supercapacitors is primarily a surface phenomenon. Furthermore, the exposure of highly reactive {110} and {100} surfaces also accounted for the high SC.

Although high surface area is crucial for charge storage, **at comparable surface areas, it is inferred that exposed crystal planes has a more profound effect on charge storage.** For instance, it can be observed from Figures 4 d) and e), despite a slightly lower surface area, CNCs exhibit higher charge storage than CNPs. The higher surface area of CNPs may facilitate it with higher EDLC type charge storage, as this type of charge storage is directly proportional to the surface area accessible to the electrolyte.^[62] However, the primary mechanism of charge storage in nano CeO₂ is pseudocapacitance.^[28, 43] Thus, CNCs, with a large exposure of high energy crystal planes that favor redox reactions, exhibited higher SC

than CNPs. From Figure 4 e) it can be seen that CNRs and CNCs consistently exhibit better rate capability than CNPs. For example, at a high current density of 8 Ag^{-1} , the SC of CNRs and CNCs reduced to 78.15 F g^{-1} and 70.74 F g^{-1} , respectively, but the SC of CNPs reduced to 38.22 F g^{-1} . This indicates that the exposure of highly reactive surfaces - $\{110\}$ and $\{100\}$ in CNRs and $\{100\}$ in CNCs equip these nanostructures with better rate performance than the low energy $\{111\}$ dominated CNPs. Table 1 lists the particle size, specific surface area, exposed planes and **specific capacitance** of all three morphologies.

Thus, our results in contrast to EDLC type material, clearly indicate that even with a high surface area, crystalline pseudocapacitive materials can yield low SC values in the absence of highly redox-active exposed crystal planes. This is in good agreement with previous reports that state surface area has a limited effect on charge storage in pseudocapacitive materials. [15, 56, 63]

The longtime cyclic performance of CNRs, CNPs, and CNCs were also evaluated. **Figure 4 f) shows the cyclic performance of the electrodes cycled for 1000 cycles in GCD at 10 A g^{-1} . All morphologies showed excellent cyclic stability with only a slight decrease in SC after 1000 continuous cycles. CNRs and CNCs showed about 90.1% and 88.3% capacitance retention. CNPs exhibited slightly lower capacitance retention at 86.4%.** The slight decrease in SC can be attributed to a number of factors. During the charge-discharge process, the active materials were exposed to repeated mechanical expansion/contraction due to the insertion/exertion of the electrolyte ions. This process could lead to the detachment of the loosely bound active material. Also, the repeated mechanical strain could force the aggregation of some nanostructures. Aggregated nanostructures would expose a lower number of redox active sites and increased internal resistance, which contribute towards the capacitance fade. [31, 43]

2.3. MD simulated Reactivity Maps of CeO_2 nanostructures

Molecular dynamics simulations were used to further understand the effect of different

exposed crystal planes on the supercapacitance of CeO₂ nanostructures. As stated previously, pseudocapacitance is linked to the ability of nano CeO₂ to be reduced. The conversion of Ce⁴⁺ to Ce³⁺ leads to the formation of oxygen vacancies. As a result, crystal planes with easily removable oxygen ions are more redox active and will offer higher redox type charge storage compared to crystal planes with strongly bound oxygen ions. Thus, it can be inferred that the amount of redox type charge storage of the crystal planes can be predicted by calculating their respective oxygen vacancy formation energies. Previous research based on Density Functional Theory (DFT) calculations have demonstrated that different surfaces possess different enthalpies of reduction. It is easier to remove oxygen from the {110} surface compared to {100} and {111} surfaces. The most stable {111} surface has the highest reduction enthalpy as expected. However, the lowest is associated with the {110} surface rather than the least stable {100} surface, which is due to a higher oxygen concentration at the {110} surfaces compared to the {100} surfaces. ^[64]

While DFT has been used to calculate the reduction energies on low index CeO₂ surfaces, the computational cost is high and therefore only perfect surfaces can be considered. Conversely, for nanoparticles and nanorods, there is considerable structural perturbation and ionic relaxation emanating from: surface steps, edges corners, point and extended defects, such as dislocations and grain boundaries. Clearly, the reduction energy at a corner site would be very different from the perfect planer surface and each atom site would likely be associated with a different reduction energy. Accordingly, to determine the reduction energy associated with a ceria nanomaterial, a model of the whole nanomaterial is required. A ceria nanomaterial 10 nm in diameter typically comprises about 30,000 atoms, which is computationally prohibitive to consider quantum mechanically. Accordingly, classical mechanics is required to capture the effect of nanostructuring on the reducibility.

Previously, we showed that the Madelung energy of surface oxygen species is correlated with the energy required to extract it (oxygen vacancy formation energy).^[65] Accordingly, the Madelung energy provides a rapid and computationally inexpensive measure of reducibility, and hence pseudocapacitance, for different nanostructures.^[66] Figures 5 a)-c) show images of the model nanoparticle, nanorod, and nanocube, colored according to their Madelung energy.^[67, 68] Visual inspection of the models reveals regions on the surfaces of the CeO₂ nanomaterials that can (energetically) be easily reduced (colored red) and regions that are relatively more difficult to reduce (colored blue). It is also evident that CNRs and CNCs have more surface sites that are redox active compared to the CNPs, which may help explain their higher specific capacitance.

In general, the simulations reveal that oxygen ions on {100} surfaces are energetically easier to remove as compared to the oxygen on {111} surfaces for both the CNPs and CNRs.^[69]^[64] This suggests that high energy {100} surfaces are more redox active than low energy {111} surfaces.^[70] It can also be observed that the corners, edges and rifts are more active than plateau {111} surfaces. We note that the CNRs and CNCs had higher proportions of {100} compared to {111} surfaces; all six of the CNCs surfaces were {100}. At comparable surface areas, the higher exposure of the more reactive planes equips CNCs with better energy storage than CNPs. Though CNCs and CNRs expose a large number of redox active crystal planes, the significantly higher surface area equips CNRs with the highest charge storage among the three nanostructures. Thus, from an energy perspective, our experimental results (SC of CNR > CNC > CNP) is supported by the simulation data that showed CeO₂ nanostructures with a higher number of {110} and {100} planes are more redox active than their {111} dominated counterparts.

We note that the reduction energies of individual Ce atoms can be very different – even on the same surface. For example, if one inspects Figure 5 b), one can see that {111} surface regions are both blue and red; some sites are easy to reduce (red), while others are energetically more

difficult (blue). This can be attributed to the structural complexity including: steps, edges, corners and ionic relaxation at curved surfaces. Such insight is currently not possible using quantum mechanical methods and therefore classical mechanics can provide unique insight. Moreover, stating that a particular (perfect) surface is reducible is overly simplistic and could even be incorrect because of the structural complexity of a nanomaterial. This argument also helps explain why a nanomaterial is catalytically more active than the parent (bulk) material that exposes reactive $\{100\}$ surfaces.

The merit of this work lies in understanding the fundamental effect of exposed crystal planes on charge storage in CeO_2 nanostructures. From electrochemical and M.D studies it is clear that exposed crystal planes play a crucial role in charge storage. It can be observed that even with a low surface area, the exposure of highly reactive crystal planes in the nanostructures leads to increased charge storage. And a combination of high surface area and exposure of highly reactive planes is needed for maximum charge storage. To the best of our knowledge, we show here for the first time, supercapacitance as evidenced by the calculated reducibility, using full atom-level models. These cost-effective MD simulations could potentially be employed to improve the charge storage performance of other crystalline material systems beyond cerium oxide.

We are cautious not to suggest that a direct correlation exists between pseudocapacitance and the relative areas of redox active surfaces because the situation is more complex. In particular, during our MD simulations, we observe some faceting of CeO_2 $\{100\}$ and $\{110\}$ surfaces into $\{111\}$ surfaces, which is thermodynamically driven to reduce the surface energy of the nanomaterial. Nevertheless, some CeO_2 $\{100\}$ and $\{110\}$ surfaces remain and the nanomaterial still has to navigate the high curvature and therefore redox active sites, such as atoms on steps, edges, and corners - are still exposed. Figures S3, S4 and S5 shows atom level models of CeO_2 nanostructures where CeO_2 $\{100\}$ and $\{110\}$ surfaces have faceted into CeO_2 $\{111\}$.

3. Experimental Section

3.1. Materials

Cerium nitrate hexahydrate ($\text{Ce}(\text{NO}_3)_3 \cdot 6\text{H}_2\text{O}$), sodium hydroxide (NaOH) and potassium hydroxide (KOH) were all purchased from Aldrich Chemical Co. (Milwaukee, WI). All reagents were used without any additional purification.

3.2. Synthesis Procedure

The procedure to selectively synthesize different morphologies, CNPs, CNRs and CNCs, uses a template free hydrothermal process by varying the caustic condition, time and temperature of the reaction. The details of which can be found in Sakthivel et al.^[52] Briefly, appropriate amounts of $\text{Ce}(\text{NO}_3)_3 \cdot 6\text{H}_2\text{O}$ and NaOH were separately mixed to 20ml of deionized water (DI H_2O). The two solutions were then mixed together with vigorous stirring. The thoroughly mixed solution was transferred to a Teflon lined stainless-steel autoclave to about 85% capacity. Finally, the sealed autoclave was placed in an electric oven and held at 80-160 °C for 6-24 h to yield different CeO_2 morphologies. After this hydrothermal process, the pale yellow precipitates (CNP or CNR) or the white precipitates (CNC) were collected, washed several times and then dried at 70°C for 12h. The schematic of the synthesis process is depicted in Figure 1a).

3.3. Electrochemical Measurements

The electrochemical measurements were performed in a three electrode configuration with 3M KOH aqueous electrolyte at room temperature. A Pt mesh and saturated Ag/AgCl (saturated NaCl) were used as the counter and reference electrode respectively. Nickel (Ni) foam was used as the current collector. Before fabricating the working electrode, the Ni foam was cleaned thoroughly by first ultrasonicing in 1M HCl for 5 min, followed by ultrasonication in ethanol for 15 min. The cleaned Ni foam was then dried and stored for future use. The working electrodes were fabricated by thoroughly mixing nano CeO_2 with

carbon black and polytetrafluoroethylene (PTFE, Alfa) in an 85:10:5 mass ratio. A small volume of N-methyl-2pyrrolidone (NMP, Alfa) was then added to this mixture to aid the formation of a homogeneous slurry. This slurry was applied on to a clean Ni foam and dried under vacuum overnight at 120°C. All working electrodes were 1 cm x 1 cm in dimension and contained approximately 2-3 mg of active material loaded. The electrochemical measurements were carried out using a potentiostat (Bio-logic). CVs were measured over a voltage range of -0.1 V to 0.45 V at sweep rates from 5 to 100 mV s⁻¹. GCDs were measured over the voltage range of -0.1 V to 0.45 V at specific currents from 1 to 32 A g⁻¹.

3.4. Instrument Characterization

The X-ray diffraction (XRD) patterns of the different CeO₂ nanostructures were acquired using a Rigaku D/MAX diffractometer with a Cu X-ray source from 15° to 80° at a scan speed of 2°/min. The shape and size of the nanostructures were analyzed using high-resolution transmission electron microscopy (HRTEM; Philips Tecnai 300kV). Surface area measurements were performed using the Brunauer–Emmett–Teller (BET) nitrogen adsorption method (*Quantachrome Nova-e* surface area analyzer). The specific surface areas of all three CeO₂ morphologies were obtained by N₂ absorption-desorption isotherms at 77 K. All surface area measurements were performed after degassing the nanostructures under vacuum at 120 °C for 8 h.

3.5. Computational Methods

Atom-level models of a ceria nanoparticle, nanorod and nanocube were generated using previously developed methods.^[71, 72] Specifically, MD simulation using the DL_POLY code,^[73, 74] was used to amorphise and then crystallize each nanostructure. Simulating crystallization enables microstructural features, such as exposed (reactive) surfaces and surface faceting, intrinsic point defects, grain-boundaries, and evolution of dislocations: all analogous to the real nanomaterial. The atoms were then colored according to their Madelung energies along a gradiented scale.^[71]

4. Conclusion

In summary, we report the influence of morphology on the supercapacitance of CeO₂ nanostructures using electrochemical techniques and molecular dynamics derived reactivity maps. Three different morphologies were synthesized by a one-step hydrothermal process. Electrochemical studies showed the supercapacitance of nanostructured CeO₂ followed the order: nano-rods > nano-cubes > nano-particles. Our findings indicate the difference in supercapacitance among the nanostructures is heavily influenced by two factors. The first is the specific surface area. A high specific surface area exposes a large number of redox active spots that facilitate pseudocapacitance type charge storage. This is clearly observed in the case of CeO₂ nano-rods, which has ~50% more surface area than the other two morphologies. The substantially high surface area facilitates CeO₂ nano-rods with the highest supercapacitance. The second is the type of the crystal plane exposed by a specific morphology. At comparable surface areas, morphologies that expose high-energy crystal planes, which are easily reduced and oxidized, exhibit higher charge storage. This was clearly observed in the case of CeO₂ nano-cubes that exhibited higher supercapacitance than CeO₂ nano-particles due to the higher exposure of the more reactive {100} planes, despite a slightly lower specific surface area. Selecting CeO₂ nano-rods over CeO₂ nano-particles could lead up to a two-fold increase in the charge storage capacity. Thus, this work provides a promise in designing supercapacitors with improved charge storage through a nanostructure morphology selection strategy.

Supporting Information

Supporting Information is available from the Wiley Online Library or from the author.

Acknowledgements

The authors would like to acknowledge the Materials Characterization Facility at the University of Central Florida for allowing us to use their characterization facilities. Dr.

Molinari acknowledges the University of Huddersfield Orion computing facility. EPSRC (EP/R010366/1, EP/H001220/1 and EP/H005838/1).

Received: ((will be filled in by the editorial staff))

Revised: ((will be filled in by the editorial staff))

Published online: ((will be filled in by the editorial staff))

References

- [1] Liu, Y.; Zhou, G. In *Key Technologies and Applications of Internet of Things*, 2012 Fifth International Conference on Intelligent Computation Technology and Automation, 2012/01//; **2012**; pp 197-200.
- [2] Yun, M.; Yuxin, B. In *Research on the architecture and key technology of Internet of Things (IoT) applied on smart grid*, 2010; IEEE: **2010**; pp 69-72.
- [3] Atzori, L.; Iera, A.; Morabito, G., *Computer Networks* **2010**, 54 (15), 2787-2805. DOI 10.1016/j.comnet.2010.05.010.
- [4] Khan, R.; Khan, S. U.; Zaheer, R.; Khan, S. In *Future Internet: The Internet of Things Architecture, Possible Applications and Key Challenges*, 2012 10th International Conference on Frontiers of Information Technology, 2012/12//; **2012**; pp 257-260.
- [5] Swan, M., *Journal of Sensor and Actuator Networks* **2012**, 1 (3), 217-253.
- [6] Curtin, T. B.; Bellingham, J. G.; Catipovic, J.; Webb, D., *Oceanography* **1993**, 6 (3), 86-94.
- [7] Vullers, R. J. M.; Van Schaijk, R.; Visser, H. J.; Penders, J.; Van Hoof, C., *IEEE Solid-State Circuits Magazine* **2010**, 2 (2), 29-38.
- [8] Weimer, M. A.; Paing, T. S.; Zane, R. A., *system* **2006**, 2 (1), 2.
- [9] Haight, R.; Haensch, W.; Friedman, D., *Science* **2016**, 353 (6295), 124-125. DOI 10.1126/science.aag0476.
- [10] Gogotsi, Y.; Simon, P., *Science* **2011**, 334 (6058), 917-918.
- [11] Simon, P.; Gogotsi, Y.; Dunn, B., *Science* **2014**, 343 (6176), 1210-1211.
- [12] Conway, B. E., *Journal of the Electrochemical Society* **1991**, 138 (6), 1539-1548.

- [13] Conway, B. E., *Electrochemical supercapacitors: scientific fundamentals and technological applications*. Springer Science & Business Media: **2013**.
- [14] Reddy, R. N.; Reddy, R. G., *Journal of Power Sources* **2003**, *124* (1), 330-337.
- [15] Chen, Z.; Augustyn, V.; Wen, J.; Zhang, Y.; Shen, M.; Dunn, B.; Lu, Y., *Advanced materials* **2011**, *23* (6), 791-795.
- [16] Brezesinski, T.; Wang, J.; Tolbert, S. H.; Dunn, B., *Nature materials* **2010**, *9* (2), 146-151.
- [17] Zhang, X.; Shi, W.; Zhu, J.; Zhao, W.; Ma, J.; Mhaisalkar, S.; Maria, T. L.; Yang, Y.; Zhang, H.; Hng, H. H., *Nano Research* **2010**, *3* (9), 643-652.
- [18] Yuan, C.; Zhang, X.; Su, L.; Gao, B.; Shen, L., *Journal of Materials Chemistry* **2009**, *19* (32), 5772-5777.
- [19] Xiong, S.; Yuan, C.; Zhang, X.; Xi, B.; Qian, Y., *Chemistry-A European Journal* **2009**, *15* (21), 5320-5326.
- [20] Simon, P.; Gogotsi, Y., *Nature Materials* **2008**, *7* (11), nmat2297. DOI 10.1038/nmat2297.
- [21] Fu, Y.; Gao, X.; Zha, D.; Zhu, J.; Ouyang, X.; Wang, X., *J. Mater. Chem. A* **2018**, *6* (4), 1601-1611. DOI 10.1039/C7TA10058B.
- [22] Bhojane, P.; Sinha, L.; Devan, R. S.; Shirage, P. M., *Nanoscale* **2018**.
- [23] Zhao, X.; Mendoza Sánchez, B.; J. Dobson, P.; S. Grant, P., *Nanoscale* **2011**, *3* (3), 839-855. DOI 10.1039/C0NR00594K.
- [24] Anasori, B.; Lukatskaya, M. R.; Gogotsi, Y., *Nature Reviews Materials* **2017**, *2* (2), natrevmats201698. DOI 10.1038/natrevmats.2016.98.
- [25] Zhou, H.; Chen, H.; Luo, S.; Lu, G.; Wei, W.; Kuang, Y., *Journal of Solid State Electrochemistry* **2005**, *9* (8), 574-580.
- [26] Acerce, M.; Voiry, D.; Chhowalla, M., *Nature Nanotechnology* **2015**, *10* (4), nnano.2015.40. DOI 10.1038/nnano.2015.40.

- [27] Zhu, Y.; Li, N.; Lv, T.; Yao, Y.; Peng, H.; Shi, J.; Cao, S.; Chen, T., *J. Mater. Chem. A* **2018**, *6* (3), 941-947. DOI 10.1039/C7TA09154K.
- [28] Brezesinski, T.; Wang, J.; Senter, R.; Brezesinski, K.; Dunn, B.; Tolbert, S. H., *ACS Nano* **2010**, *4* (2), 967-977. DOI 10.1021/nn9007324.
- [29] Heydari, H.; Gholivand, M. B., *Applied Physics A* **2017**, *123* (3), 187.
- [30] Dezfuli, A. S.; Ganjali, M. R.; Naderi, H. R.; Norouzi, P., *RSC Advances* **2015**, *5* (57), 46050-46058.
- [31] Kumar, R.; Agrawal, A.; Nagarale, R. K.; Sharma, A., *The Journal of Physical Chemistry C* **2016**, *120* (6), 3107-3116.
- [32] Tao, Y.; Ruiyi, L.; Haiyan, Z.; Zaijun, L., *Materials Research Bulletin* **2016**, *78*, 163-171.
- [33] Corma, A.; Atienzar, P.; García, H.; Chane-Ching, J.-Y., *Nature materials* **2004**, *3* (6), 394-397.
- [34] Karakoti, A.; Singh, S.; Dowding, J. M.; Seal, S.; Self, W. T., *Chemical Society Reviews* **2010**, *39* (11), 4422-4432.
- [35] Trovarelli, A., *Catalysis Reviews* **1996**, *38* (4), 439-520.
- [36] Montini, T.; Melchionna, M.; Monai, M.; Fornasiero, P., *Chemical reviews* **2016**, *116* (10), 5987-6041.
- [37] Sayle, D. C.; Seal, S.; Wang, Z.; Mangili, B. C.; Price, D. W.; Karakoti, A. S.; Kuchibhatla, S. V. T. N.; Hao, Q.; Mobus, G.; Xu, X., *ACS Nano* **2008**, *2* (6), 1237-1251.
- [38] Sayle, D. C.; Feng, X.; Ding, Y.; Wang, Z. L.; Sayle, T. X. T., *Journal of the American Chemical Society* **2007**, *129* (25), 7924-7935.
- [39] Aravinda, L. S.; Bhat, K. U.; Bhat, B. R., *Materials Letters* **2013**, *112*, 158-161.
- [40] Ji, Z.; Shen, X.; Zhou, H.; Chen, K., *Ceramics International* **2015**, *41* (7), 8710-8716.
- [41] Kalubarme, R. S.; Kim, Y.-H.; Park, C.-J., *Nanotechnology* **2013**, *24* (36), 365401.
- [42] Maheswari, N.; Muralidharan, G., *Energy & Fuels* **2015**, *29* (12), 8246-8253.

- [43] Padmanathan, N.; Selladurai, S., *RSC Advances* **2014**, *4* (13), 6527-6534.
- [44] Maiti, S.; Pramanik, A.; Mahanty, S., *Chemical Communications* **2014**, *50* (79), 11717-11720.
- [45] Kyeremateng, N. A.; Brousse, T.; Pech, D., *Nature Nanotechnology* **2016**, *12* (1), nnano.2016.196. DOI 10.1038/nnano.2016.196.
- [46] Liu, X.; Liu, J.; Chang, Z.; Sun, X.; Li, Y., *Catalysis Communications* **2011**, *12* (6), 530-534.
- [47] Wang, Y.; Zhong, Z.; Chen, Y.; Ng, C. T.; Lin, J., *Nano Research* **2011**, *4* (7), 695. DOI 10.1007/s12274-011-0125-x.
- [48] Xiao, X.; Liu, X.; Zhao, H.; Chen, D.; Liu, F.; Xiang, J.; Hu, Z.; Li, Y., *Advanced Materials* **2012**, *24* (42), 5762-5766. DOI 10.1002/adma.201202271.
- [49] Mai, H.-X.; Sun, L.-D.; Zhang, Y.-W.; Si, R.; Feng, W.; Zhang, H.-P.; Liu, H.-C.; Yan, C.-H., *The Journal of Physical Chemistry B* **2005**, *109* (51), 24380-24385.
- [50] Huang, W.; Gao, Y., *Catalysis Science & Technology* **2014**, *4* (11), 3772-3784.
- [51] Sayle, T. X. T.; Parker, S. C.; Catlow, C. R. A., *Surface Science* **1994**, *316* (3), 329-336. DOI 10.1016/0039-6028(94)91225-4.
- [52] Sakthivel, T.; Das, S.; Kumar, A.; Reid, D. L.; Gupta, A.; Sayle, D. C.; Seal, S., *ChemPlusChem* **2013**, *78* (12), 1446-1455. DOI 10.1002/cplu.201300302.
- [53] Chang, J.; Lee, W.; Mane, R. S.; Cho, B. W.; Han, S.-H., *Electrochemical and Solid-State Letters* **2008**, *11* (1), A9-A11.
- [54] Choi, D.; Blomgren, G. E.; Kumta, P. N., *Advanced Materials* **2006**, *18* (9), 1178-1182.
- [55] Mai, L.-Q.; Yang, F.; Zhao, Y.-L.; Xu, X.; Xu, L.; Luo, Y.-Z., *Nature communications* **2011**, *2*, ncomms1387.
- [56] Kim, J. W.; Augustyn, V.; Dunn, B., *Advanced Energy Materials* **2012**, *2* (1), 141-148.

- [57] Wang, J.; Polleux, J.; Lim, J.; Dunn, B., *The Journal of Physical Chemistry C* **2007**, *111* (40), 14925-14931.
- [58] Yan, J.; Fan, Z.; Sun, W.; Ning, G.; Wei, T.; Zhang, Q.; Zhang, R.; Zhi, L.; Wei, F., *Advanced Functional Materials* **2012**, *22* (12), 2632-2641.
- [59] Kong, L.-B.; Lang, J.-W.; Liu, M.; Luo, Y.-C.; Kang, L., *Journal of Power Sources* **2009**, *194* (2), 1194-1201.
- [60] Dubal, D. P.; Fulari, V. J.; Lokhande, C. D., *Microporous and Mesoporous Materials* **2012**, *151*, 511-516.
- [61] Gund, G. S.; Dubal, D. P.; Patil, B. H.; Shinde, S. S.; Lokhande, C. D., *Electrochimica Acta* **2013**, *92*, 205-215.
- [62] González, A.; Goikolea, E.; Barrena, J. A.; Mysyk, R., *Renewable and Sustainable Energy Reviews* **2016**, *58*, 1189-1206.
- [63] Ghodbane, O.; Pascal, J.-L.; Favier, F., *ACS applied materials & interfaces* **2009**, *1* (5), 1130-1139.
- [64] Molinari, M.; Parker, S. C.; Sayle, D. C.; Islam, M. S., *The Journal of Physical Chemistry C* **2012**, *116* (12), 7073-7082.
- [65] Sayle, T. X. T.; Molinari, M.; Das, S.; Bhatta, U. M.; Möbus, G.; Parker, S. C.; Seal, S.; Sayle, D. C., *Nanoscale* **2013**, *5* (13), 6063-6073. DOI 10.1039/C3NR00917C.
- [66] Sayle, T. X. T.; Cantoni, M.; Bhatta, U. M.; Parker, S. C.; Hall, S. R.; Möbus, G.; Molinari, M.; Reid, D.; Seal, S.; Sayle, D. C., *Chem. Mater.* **2012**, *24* (10), 1811-1821. DOI 10.1021/cm3003436.
- [67] Watson, G. W., *Chem. Soc. Faraday Trans* **1996**, *92*, 433-438.
- [68] Smith, W.; Forester, T. R., *Journal of molecular graphics* **1996**, *14* (3), 136-141.
- [69] Conesa, J., *Surface Science* **1995**, *339* (3), 337-352.
- [70] Nolan, M.; Grigoleit, S.; Sayle, D. C.; Parker, S. C.; Watson, G. W., *Surface Science* **2005**, *576* (1), 217-229. DOI 10.1016/j.susc.2004.12.016.

- [71] Feng, X.; Sayle, D. C.; Wang, Z. L.; Paras, M. S.; Santora, B.; Sutorik, A. C.; Sayle, T. X. T.; Yang, Y.; Ding, Y.; Wang, X., *Science* **2006**, *312* (5779), 1504-1508.
- [72] Caddeo, F.; Corrias, A.; Sayle, D. C., *The Journal of Physical Chemistry C* **2016**, *120* (26), 14337-14344. DOI 10.1021/acs.jpcc.6b02279.
- [73] Sayle, T. X. T.; Parker, S. C.; Sayle, D. C., *Chemical Communications* **2004**, (21), 2438-2439.
- [74] Sayle, D. C.; Maicananu, S. A.; Watson, G. W., *Journal of the American Chemical Society* **2002**, *124* (38), 11429-11439.

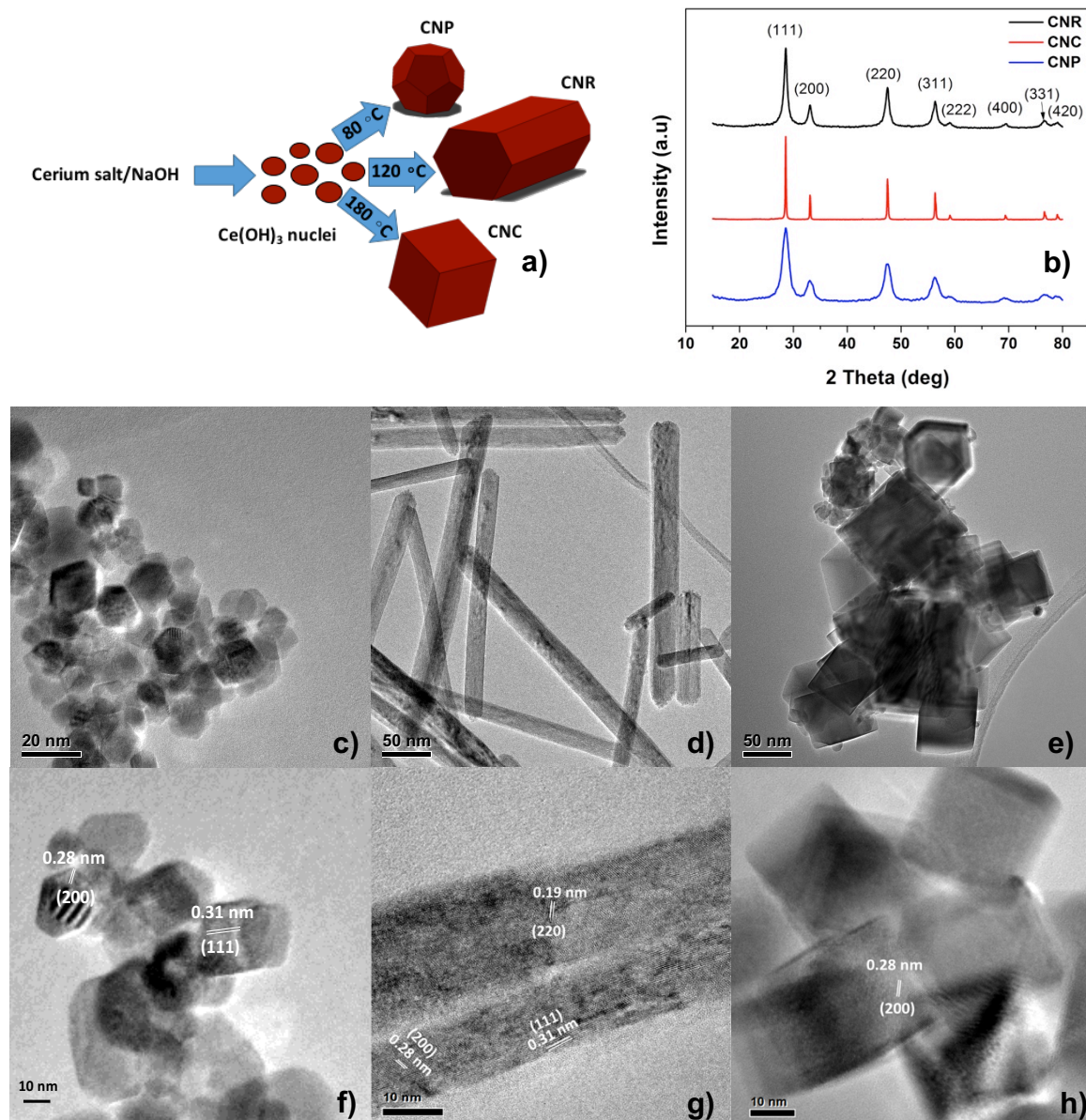


Figure 1. Synthesis and physical characterization of different CeO₂ nanostructures. a) Synthesis schematics of CeO₂ nanostructures through a one-step hydrothermal technique. b) XRD patterns of CNR, CNC and CNP. c)-e) TEM images and f)-h) HRTEM images of CNP, CNR, and CNC, respectively.

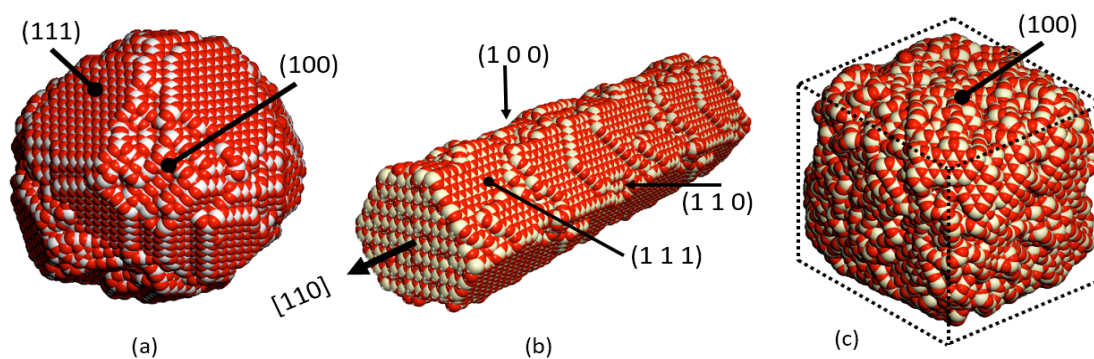


Figure 2. Atomistic models of CeO₂ nanostructures generated by MD simulations. Ce atoms colored white and oxygen colored red. MD simulation revealed a) CNP exhibits an octahedral morphology with {111} truncated by {100} surfaces. b) CNRs are enclosed by {100} and {110} surfaces and show a unidirectional growth in the [110] direction. c) CNCs exposed six {100} surfaces. The MD simulations are in good agreement with TEM images.

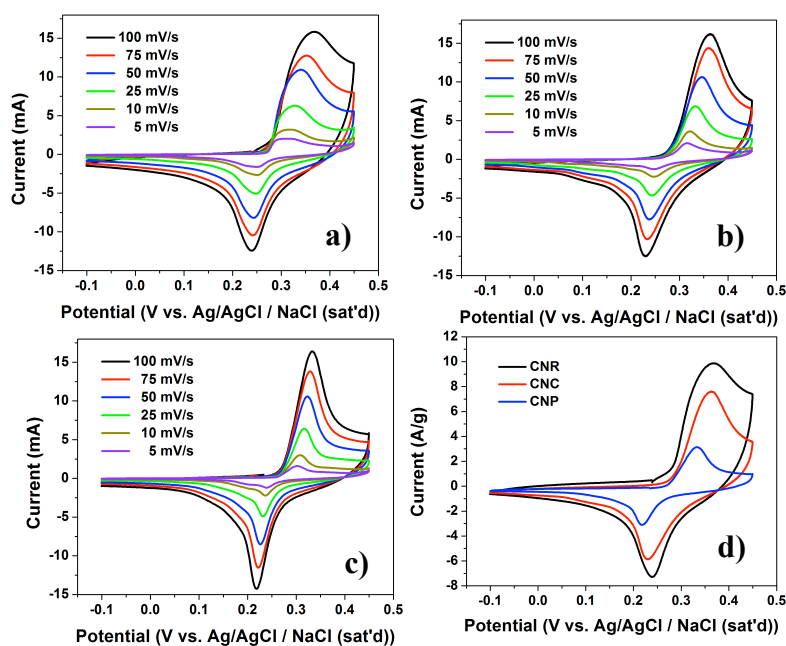


Figure 3. Electrochemical characterization of CeO₂ nanostructures in 3M KOH. CV curves of a) CNRs, b) CNCs and c) CNPs at potential scan rates from 5 mV s⁻¹ to 100 mV s⁻¹. d) Comparison of the CV curves of the three morphologies at a scan rate of 100 mV s⁻¹. The SC shows a strong dependence on morphology and followed the order: SC of CNR > CNC > CNP.

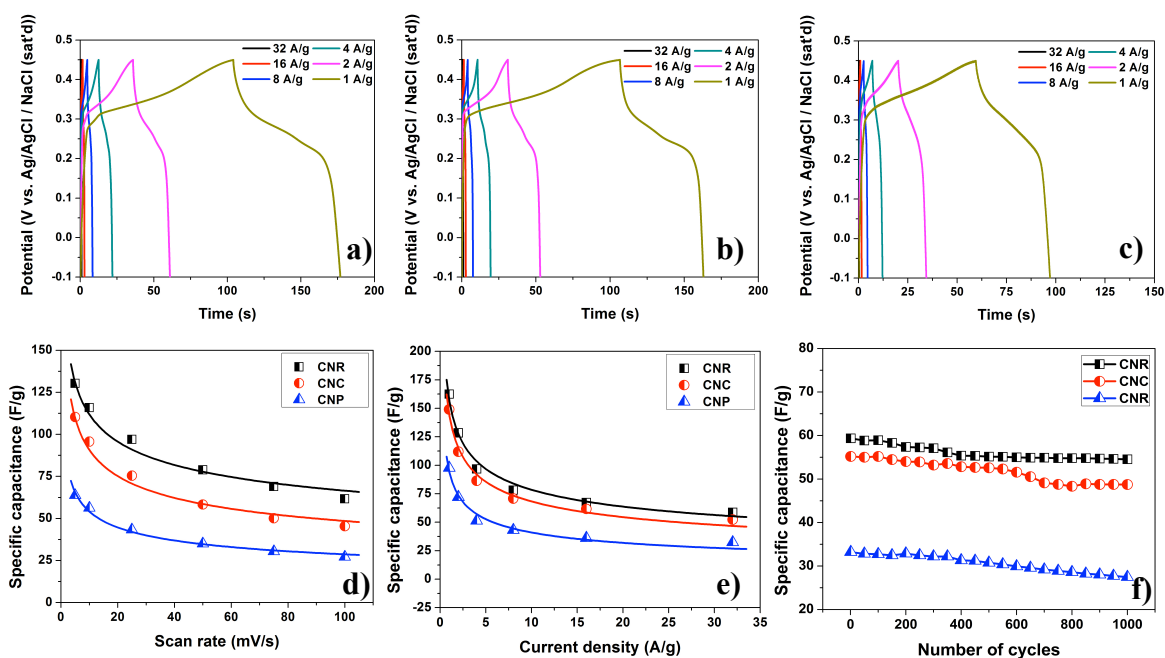


Figure 4. Supercapacitor performance of CeO₂ nanostructures. Galvanostatic charge discharge curves of a) CNRs, b) CNCs and c) CNPs, at current densities from 1 A g⁻¹ to 32 A g⁻¹. Specific capacitance of CeO₂ nanostructures as a function of d) scan rate and e) current density. f) Cyclic performance of CeO₂ nanostructures at 10 A g⁻¹. The higher SC of CNRs can be attributed to the large difference in surface area and high exposure of the more redox active {100} and {100} surfaces. Though CeO₂ nano-cubes and CeO₂ nano-particles have comparable specific surface areas, the high exposure of more active {100} facets in CeO₂ nano-cubes facilitate them with higher SC.

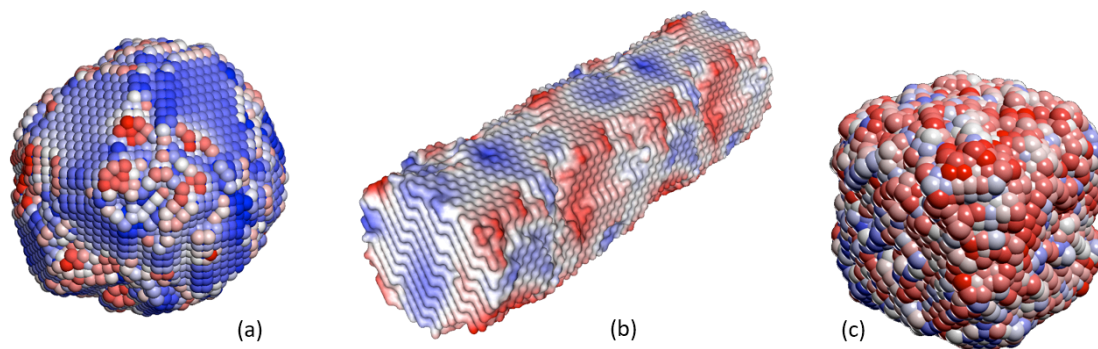


Figure 5. Reactivity maps of nanostructures predicted through Madelung energy. a) CNPs, b) CNCs and c) CNPs. Atoms colored according to calculated Madelung energy – red-white-blue gradient scale indicates low to high Madelung energy. The image shows that atoms on the {100} surfaces have predominantly low Madelung energies, which indicates they are more easily reduced compared to ions on the {111} surface. It can be observed that corners and edges are more reactive than the plateau {111} surface.

Table 1. Summary of the characterization performed on three different nano CeO₂ nanostructures.

	CeO ₂ nano-rods	CeO ₂ nano-cubes	CeO ₂ nano-particle
TEM particle size [nm]	W 10-20 L 100-200	20-40	15-20
Specific surface area [m ² g ⁻¹]	61.18	38.27	44.01
Exposed planes	{100} + {110} + {111}	{100}	{111} + {100}
Specific capacitance @1A/g [F g ⁻¹]	162.47	149.03	87.73